Intracellular mechanics and TBX3 expression jointly dictate the spreading mode of melanoma cells in 3D environments

Ghodeejah Higgins[1], Faatiemah Higgins[2], Jade Peres[2], Dirk M Lang[2], Tamer Abdalrahman[1], Muhammad H. Zaman[3,4], Sharon Prince[2], Thomas Franz[1]*

[1]Division of Biomedical Engineering, Department of Human Biology, University of Cape Town, Observatory, South Africa

[2]Division of Cellular, Physiological and Nutritional Sciences, Department of Human Biology, University of Cape Town, Observatory, South Africa

[3]Department of Biomedical Engineering, Boston University, Boston, MA, USA

[4]Howard Hughes Medical Institute, Chevy Chase, MD, USA

Running title: Melanoma stiffness & TBX3 in 3D

ORCID

G Higgins: 0000-0003-3576-9031

F Higgins: 0000-0002-2389-2625

J Peres: 0000-0001-8568-4840

DM Lang: 0000-0003-3901-2079

T Abdalrahman: 0000-0002-0320-811X

MH Zaman: 0000-0002-3723-5431

S Prince: 0000-0002-6975-5255

T Franz: 0000-0002-1504-3842

*Corresponding author: Thomas Franz, thomas.franz@uct.ac.za

Summary statement

Effects of cell stiffness, mitochondrial activity and TBX3 expression on cluster formation, which are dependent on environmental stiffness, may jointly aid in site-specific melanoma therapies.

Abstract

Cell stiffness and TBX3 expression have been identified as biomarkers of melanoma metastasis in 2D environments. This study aimed to determine how mechanical and biochemical properties of melanoma cells change during cluster formation and metastasis in 3D environments mimicking physiological conditions. In isolated cells, mitochondrial fluctuations decreased, and stiffness increased across disease stages and matrix rigidities. TBX3 was overexpressed in soft but diminished in stiff matrices. During cluster formation in soft matrices, the intracellular properties of VGP cells did not change during extensive cluster formation, whereas mitochondrial fluctuations increased and TBX3 expression decreased in MET cells during limited cluster formation. In stiff matrices, cluster formation was restricted, mitochondrial fluctuations and TBX3 expression increased in VGP and MET, and cell stiffness increased in VGP and decreased in MET. Mitochondrial activity, cell stiffness, and TBX3 expression jointly affected cluster formation and metastasis in melanoma, with contributions varying with environmental properties. Hence, biomechanical and biochemical properties of the cells and the environment should be combined to advance targeted cancer therapies.

Keywords:

Cluster formation, cluster morphology, mitochondrial particle tracking microrheology, cell mechanics, T-box factors, collagen

1. Introduction

Each step of the metastatic cascade is bioenergetically demanding and requires the biomechanical adjustment of cell volume and shape and hence, altered biochemical cascades (Fife et al., 2014) and changing cell mechanical properties (Northcott et al., 2018).

Recently, cell mechanical properties have emerged as potential biomarkers of cancer malignancy. Compared to normal cells, isolated cancer cells generate increased contractile forces (Mierke et al., 2008) and are more deformable (Agus et al., 2013). In contrast, solid cancer tumours are more rigid than normal tissue (Taubenberger et al., 2019). However, biomechanical changes in cells as they evolve from isolated cells into tumours have not been reported.

It is known that melanoma cells prefer distant metastasis in the lung, liver, brain, and bone (Damsky et al., 2010). However, little is known about why melanoma cells may favour specific distant organs over others. Even less is known about the melanoma cell's inherent biomechanical and biochemical properties that coordinate tumour formation in changing 3D environments, particularly at an advanced melanoma stage.

TBX3, a member of the T-box family of transcription factors, has recently emerged as a potential molecular biomarker of melanoma metastasis (Peres and Prince, 2013). Overexpressed TBX3 has been shown to impart oncogenic properties in cells, such as uncontrolled proliferation, tumour formation, migration and invasion, and metastasis (Khan et al., 2020). For example, a recent study showed that the elevation of TBX3 levels in non-tumorigenic radial growth phase (RGP) melanoma cells stimulated tumour formation and enhanced migration and invasion in 2D *in vitro* and mouse *in vivo* models (Peres and Prince, 2013).

The molecular mechanisms that upregulate TBX3 are currently not well understood, and even less is known about the mechanical mediators of TBX3 regulation, such as changes in matrix rigidity. Notably, TBX3 research has been primarily conducted in 2D *in vitro* conditions or *in vivo* in animal models. However, cells grown on rigid 2D substrates are not physiologically relevant and fail to accurately depict complex cell-cell and cell-matrix interactions (Wullkopf et al., 2018). In contrast, *in vivo* animal models better mimic physiologically relevant cell-cell and cell-matrix interaction. However, *in vivo* environments are spatially complex, and it is currently challenging to control precise cues from the microenvironment, such as properties of the extracellular matrix (Cavo et al., 2016). Furthermore, it is unclear how TBX3 is

expressed in advanced melanoma cells in 3D *in vitro* models and how TBX3 expression changes with melanoma progression, increased matrix rigidity or cluster formation.

Therefore, this study aimed to determine how: (i) biomechanical mediators, including intracellular stiffness and matrix rigidity, affect cluster formation of advanced melanoma, and (ii) TBX3 levels change in melanoma cells with different cluster formation characteristics before and after cluster formation in 3D *in vitro* collagen matrices of varying rigidity.

2. Results

2.1. Morphology

2.1.1. VGP isolated cells and cell clusters were larger than MET counterparts

Morphology measurements were obtained from 28 images from three repeat experiments (n = 4).

For absolute cell area, the advanced disease stage (MET versus VGP) exhibited a marked decrease of the predicted area $\hat{A}$ on Day 1 and Day 4 ($p < .001$ and $p = .001$, respectively) and a slight decrease of $\hat{A}$ on Day 7 and Day 10 ($p = .254$ and $p = .168$, respectively) , Figure 1a. Increased collagen concentration from 2 to 4 mg/ml correlated with a decrease of $\hat{A}$ of cells on Day 1 ($p = .004$). For cell clusters, increased collagen concentration correlated with a decrease of $\hat{A}$ on Day 4 and 7 ($p = .435$ and $p = .512$, respectively), although this was not significant, and had no effect on $\hat{A}$ on Day 10 ($p = .740$).

For normalized cluster area, advanced disease stage correlated with a decrease in $\hat{A}_N$ on Day 4 and Day 7 ($p < .001$ and $p =.001$, respectively) but did not alter $\hat{A}_N$ on Day 10 ($p = .222$). Increased collagen concentration correlated with a decrease in $\hat{A}_N$ on Day 4 and Day 7 ($p = .154$ and $p = .616$, respectively), although not significant, and did not alter $\hat{A}_N$ on Day 10 ($p = .990$).

Finally, increased time points from Day 1 to Day 4, 7 and 10, respectively, correlated with an increase of $\hat{A}$ and $\hat{A}_N$ ($p < .001$ for all cases), indicating cluster growth.

Pairwise comparisons indicated that the absolute area was larger for VGP cells than for MET cells at each time point and for both collagen concentrations ($p < .001$). However, when normalized, VGP clusters were larger than MET clusters on Days 4 and 7 in 2 mg/ml ($p < .001$ for both cases) and in 4 mg/ml collagen ($p < .001$ and $p = .002$, respectively). For Day

10, VGP and MET clusters had similar normalized area in 2 and 4 mg/ml collagen (p = .085 and p = .008, respectively). To account for multiple comparison testing, Bonferroni correction led to significance at $p < .006$.

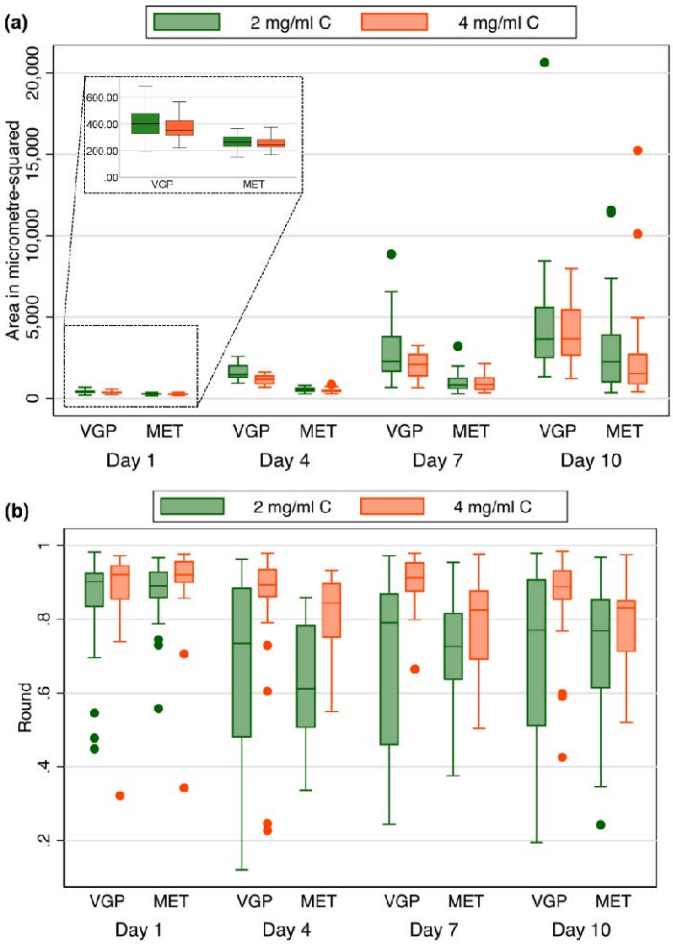

Figure 1: Morphology of VGP and MET cells over 10 days. (a) VGP cells exhibited a larger area A than MET cells ($p < .001$) for all time points and collagen concentrations. (b) Isolated VGP and MET cells on Day 1 were round ($R \geq 0.8$) irrespective of the collagen concentration of the matrix. VGP and MET cell clusters were mostly elongated ($R < 0.8$) for 2 mg/ml collagen concentration (C) and round for 4 mg/ml collagen concentration.

2.1.2. Roundness of cell clusters increased with increased collagen concentration

Isolated cells and cell clusters were considered round for median roundness $R \geq 0.80$ and elongated for $R < 0.80$ (Figure 1b). Isolated VGP and MET cells (Day 1) were predominantly round, regardless of collagen concentration, with some notably elongated cells (outliers). In comparison, VGP and MET cell clusters were mostly elongated in 2 mg/ml collagen and round in 4 mg/ml collagen (Figure 2).

A beta regression model showed that an increase in time from Day 1 to 4, 7 and 10, respectively ($p < .001$, $p = .002$, and $p = .006$, respectively), correlated with a decrease in □. In contrast, an increase in collagen concentration from 2 to 4 mg/ml correlated with an increase in □ on Day 4 and 7 ($p = .045$ and $p = .019$, respectively) but did not contribute to changes in □ on Day 1 and Day 10 ($p = .327$ and $p = .132$, respectively).

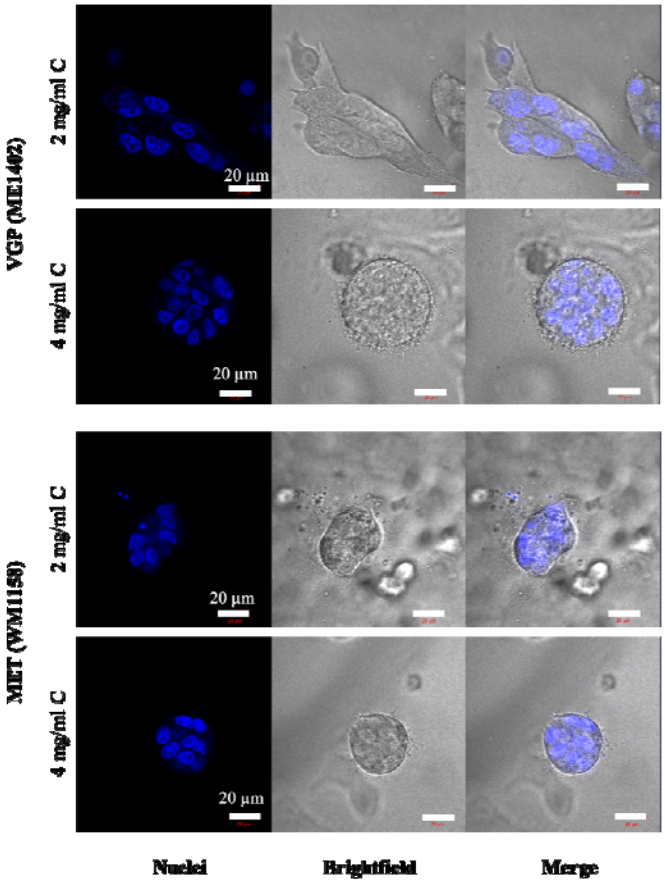

Figure 2: Confocal images (2D confocal plane) of VGP and MET clusters after 7 days in 2 and 4 mg/ml collagen (C) matrices. Each panel presents fluorescently labelled nuclei (blue)(left), brightfield (middle) and merged image (right). In 2 mg/ml C, the elongated shape was more defined for VGP clusters than MET clusters. Increased collagen concentration compacted and rounded the cell clusters. (All images 63x magnification, scale bar represents 20 µm).

2.2. Structural properties of cell clusters

The actin cytoskeleton is vital in controlling global cell morphology and structure (Chugh and Paluch, 2018). Cell clusters on Day 7 were processed for immunofluorescence to detect F-actin and visualized by confocal microscopy.

2.2.1. Elongated VGP clusters formed supracellular features, and large VGP clusters merged from smaller clusters

Elongated VGP clusters were categorized as sharp- or blunt-edged in 2 mg/ml collagen (Figure 3a, b). Sharp-edged clusters comprised mostly large, elongated cells that formed supracellular features, such as supracellular protrusive fronts and retracting tails (Figure 3a, blue arrows). Elongated clusters with a blunt edge showed no supracellular protrusions;

however, microspikes were present. More importantly, 2D planes showed clear borders outlining at least two clusters that had merged into one cluster (see dashed lines in Figure 3b).

Interestingly, actin visualization demonstrated merged VGP clusters in 2 mg/ml collagen (Figure 3c). Thick actin bundles (white arrow) were apparent at the interface of merged clusters.

Round VGP clusters exhibited similar actin-filled pseudopodia in 2 and 4 mg/ml collagen (Figure 3c, d). Several filopodia and microspikes emanated from cells at the cluster surface. Many clusters in 4 mg/ml collagen consisted of a single large and round cell ($R > 0.90$) with a thick actin cortex in the cluster's interior. This cell was more than twice the size of neighbouring cells.

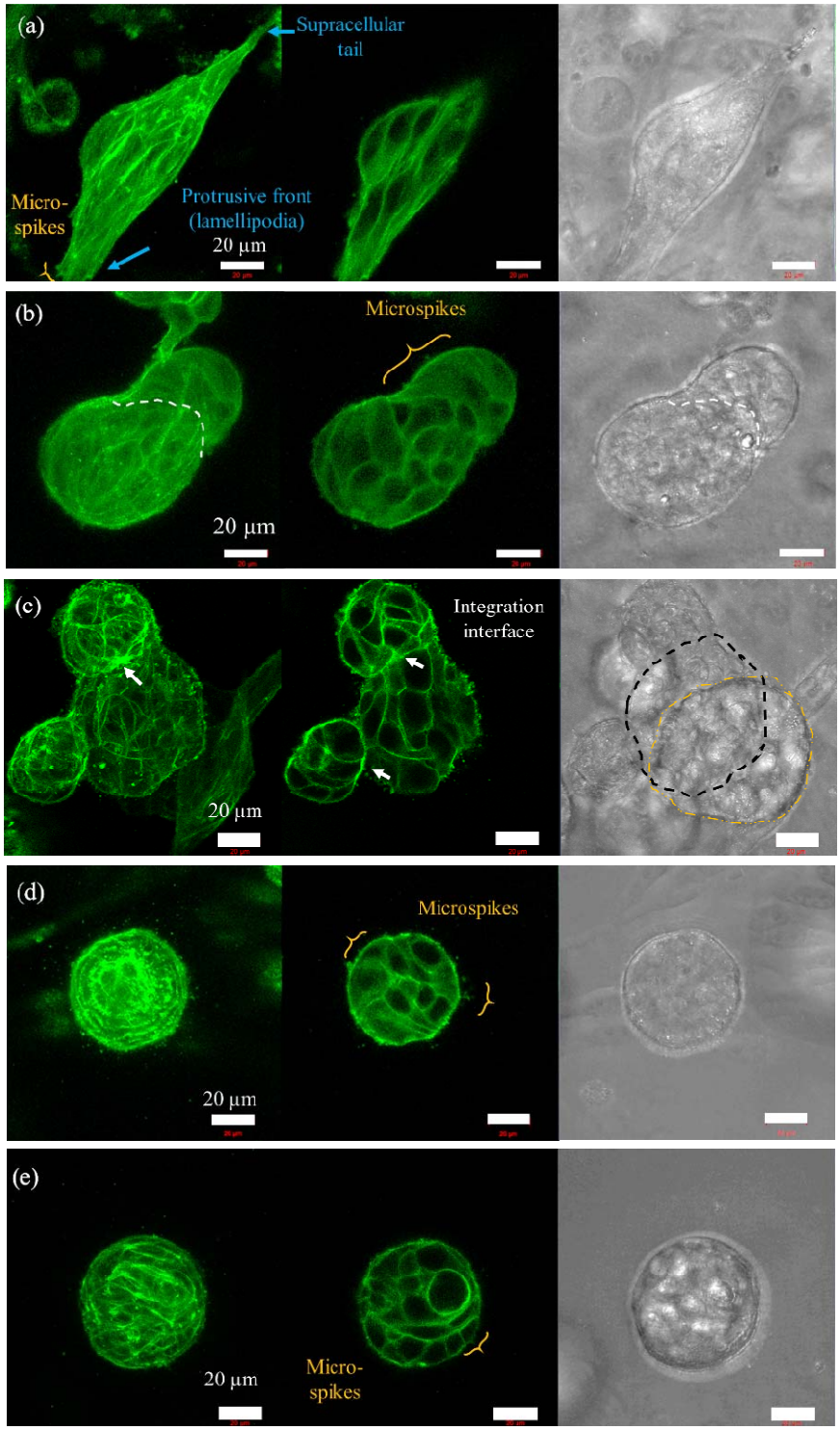

Figure 3: Confocal images of elongated (a, b), merged (c), and rounded (d, e) VGP cell clusters after 7 days in 2 and 4 mg/ml collagen matrices. Each panel shows the mean intensity projection (MIP) of multiple fluorescently labelled F-actin (green) of confocal image stacks (left), F-actin of the mid-2D plane (middle) and MIP of brightfield confocal image stacks (right). All images at 63x magnification; scale bar represents 20 µm. (a,b) Elongated VGP clusters were distinguished by sharp or blunt edges in 2 mg/ml

collagen. Sharp-edged cluster (a) exhibiting supracellular edge features, i.e. protrusive front and retracting tail (blue arrows and text). Microspikes (gold bracket) were visible on the protrusions. Blunt-edge cluster (b) merged from two smaller clusters (white dashed line shows the merging site).
(c) Merged clusters resulted from two or more cell clusters that migrated towards each other and merged in 2 mg/ml collagen. The interface of merged clusters (white arrows) consisted of thick F-actin bundles in fluorescence images. The merged interface in (c) is outlined (black dashed curve) in brightfield images to distinguish it from the separate cluster not part of the merged cluster. Yellow dashed curve outlines a separate cluster that appeared in the field of view but is not attached to the merged cluster.
(d, e) For round VGP clusters in 2 mg/ml collagen (d) and 4 mg/ml collagen (e), pseudopodia were primarily in the form of finger-like protrusions. Most of the round clusters in 4 mg/ml C contained a large cell towards the cluster interior.

2.2.2. MET clusters exhibited several types of pseudopodia in 2 mg/ml collagen but were only in the form of filopodia in 4 mg/ml collagen

MET clusters invaded the 2 mg/ml collagen environment as either loose (i.e. non-adherent) or compact cell groups. In loose MET clusters, the first cell in the cluster, the leader cell, had a planar protrusive front. All cells had a retracting tail (see blue arrows in Figure 4a). Each cell within the cluster exhibited a thick actin cortex, and filopodia and microspikes emanating from the cell membrane. The thickest actin cortex and the most prominent filopodia and microspikes were observed in the leader cell (Figure 4a).

Compact MET clusters were either elongated or round in 2 mg/ml collagen, as in VGP clusters, and mostly round in 4 mg/ml collagen. Elongated compact clusters formed supracellular planar protrusive front and retracting tails (Figure 4b). Round MET clusters extended varying pseudopodia, with a complexity that depended on matrix rigidity. In 2 mg/ml collagen, round MET clusters exhibited branching filamentous pseudopodal networks, known as reticulopodia, and several filopodia (Figure 4c). In 4 mg/ml collagen, long filopodia and short microspikes were present (Figure 4d).

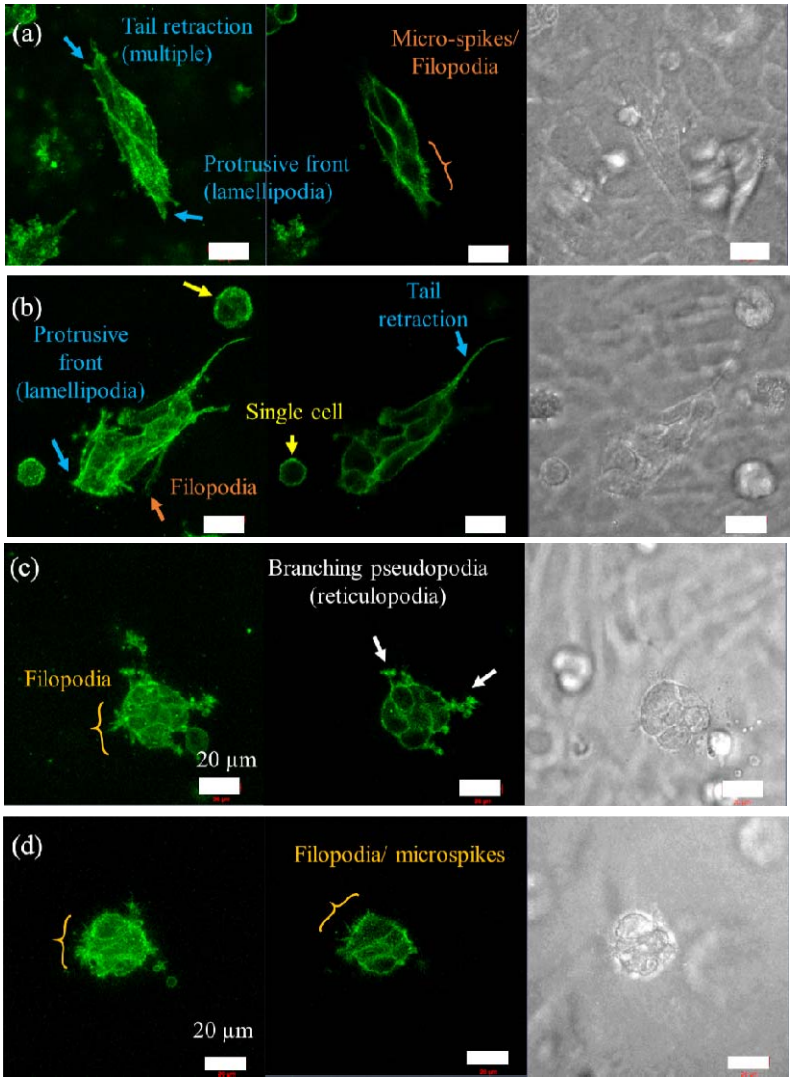

Figure 4: Confocal images of elongated (a, b) and round (c, d) MET cell clusters after 7 days in 2 and 4 mg/ml collagen matrices. Each panel shows the mean intensity projection (MIP) of multiple fluorescently labelled F-actin (green) of confocal image stacks (left), F-actin of the mid-2D plane (middle) and MIP of brightfield confocal image stacks (right). All images at 63x magnification; scale bar represents 20 µm.
(a, b) Elongated MET clusters were either loose or compact in 2 mg/ml collagen. (a) Loose clusters comprised cells aligned with each other. Each cell in the cluster featured one retracting tail (blue arrow and label). (b) Compact elongated clusters emerged as supracellular units with a protrusive front and retracting tails (blue arrows and label). Single cells in the cluster's vicinity were polarised as indicated by the focalized F-actin in the cortex (yellow arrow and label). Slender filopodia and microspikes are indicated with orange arrows, respectively.
(c, d) Rounded MET clusters exhibited complex branching pseudopodia (white arrows) and filopodia (orange bracket) in 2 mg/ml collagen (c) compared to simple filopodia and microspikes in 4 mg/ml collagen (d).

2.3. Mechanical properties

Mitochondrial particle tracking experiments were conducted to investigate the intracellular mechanics of isolated cells and cell clusters. Mitochondrial fluctuations were traced and used to calculate the mean squared displacement (MSD) and power-law coefficient α.

Low MSD values correspond to inhibited particle displacement and indicate stiffer, solid materials whereas high MSDs indicate a greater particle motility and a softer, more fluid-like material. The MSD was determined for different delay times τ, i.e. the period between the first and the last image frame used for the analysis. Particles may displace small amounts due to random forces from the surrounding medium's thermal energy during short delay times, or displace large amounts due to active, motor-driven processes at large delay times (Guo et al., 2014; Kim et al., 2018; Mak et al., 2014).

The power-law coefficient α (representing the slope of the logarithmic MSD-delay time curve) characterises the power-law delay time dependence and helps classifying the motion of the tracer particles. An α close to 1 corresponds to diffusive motion such as thermal fluctuations in a Newtonian fluid whereas an α close to 0 indicates constrained, sub-diffusive motion such as thermal fluctuations in an elastic material (Kim et al., 2018; Mason et al., 1997). Mitochondrial particles typically experience considerable intracellular traffic and therefore undergo constrained, sub-diffusive particle fluctuation with $0 < \alpha < 1$, which can be further classified into strong ($0 < \alpha < 0.3$) or weak ($0.7 < \alpha < 1$) sub-diffusive motion.

Lower and flat MSD-τ curves (e.g. Figure 5 b-d) indicate solid-like intracellular behaviour whereas higher and increasingly sloped curves indicate more fluid-like, intracellular motor-driven mechanics.

2.3.1. VGP were more deformable than MET isolated cells

For isolated cells, the MSD and power-law coefficient α were larger for VGP cells than for MET cells in 2 and 4 mg/ml collagen matrices at short (MSD at $\tau = 0.05$ s and α at $\tau = 1$ s), intermediate (MSD and α at $\tau = 3$ s), and large delay times (MSD and α at $\tau = 5$ s), see Figure 5(a) and Table S1.

The MSD and α of isolated VGP cells were similar in 2 and 4 mg/ml collagen matrices for all delay times τ. For MET cells, the MSD of cells in 4 mg/ml collagen compared to cells in 2 mg/ml collagen increased with delay times, with statistical significance indicated for $\tau \geq 5$ s. α of MET cells decreased for increased collagen concentration for all delay times (Figure 5a).

A decrease in MSD and α, respectively, indicated that mitochondrial fluctuations were impeded and cells changed from fluid- to solid-like behaviour.The more advanced MET disease stage exhibited decreased mitochondrial fluctuations and increased cell stiffness of isolated cells in 2 and 4 mg/ml collagen (Figure 5b - e). Increased collagen concentration correlated with decreased mitochondrial fluctuations and increased cell stiffness for MET but not VGP cells.

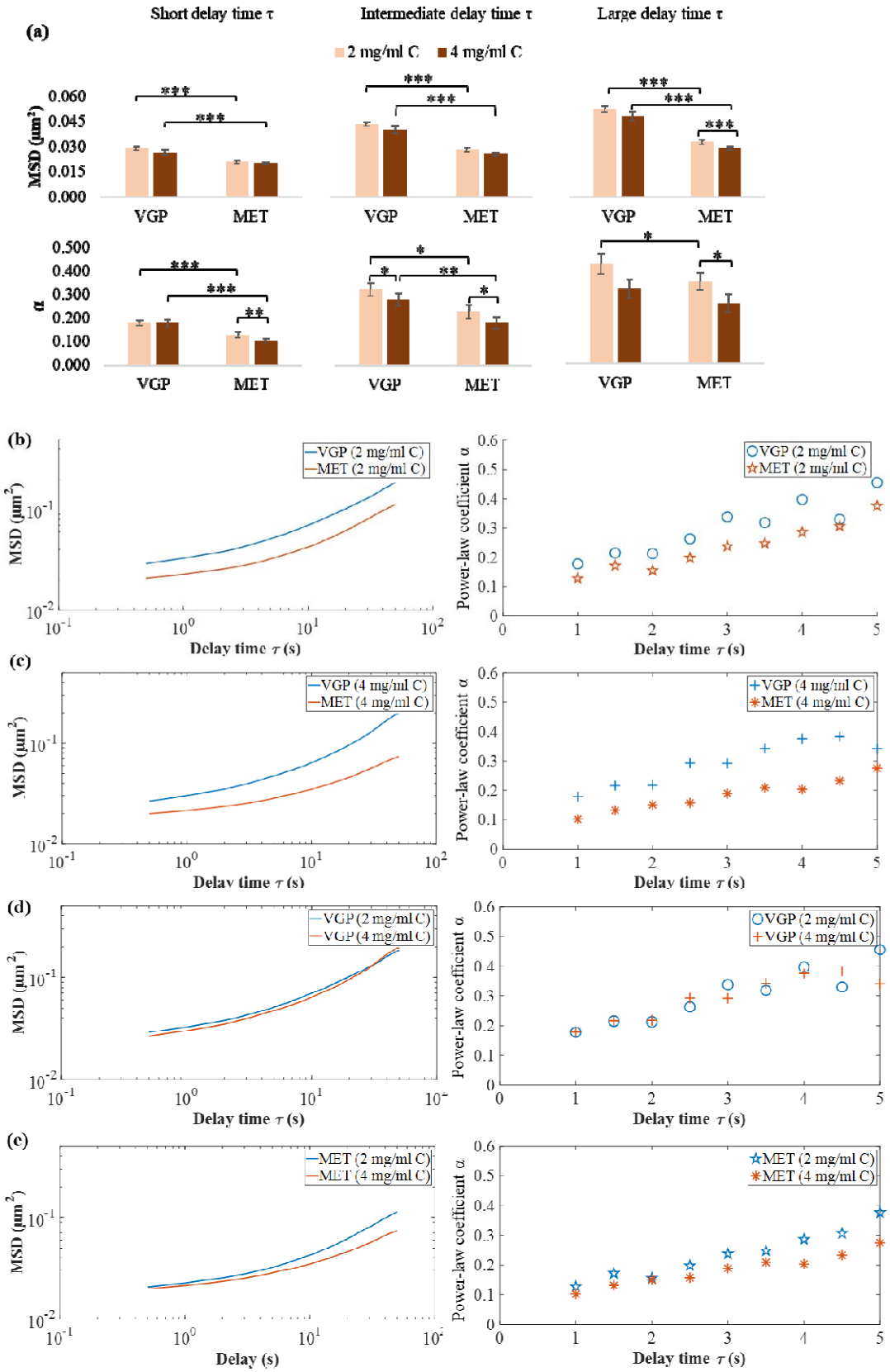

Figure 5: MSD and power-law coefficient α of VGP and MET ***isolated cells*** *(i.e. at Day 1) in*

matrices with 2 and 4 mg/ml collagen concentration (C). a) Comparison of disease stage and collagen concentration at short (MSD: $\tau = 0.05$ s, α: $\tau = 1$ s), intermediate (MSD and α: $\tau = 3$ s) and long delay time (MSD and α: $\tau = 5$ s). b, c) Comparison of different disease stages for the same collagen concentration. MET cells had lower MSD and α than VGP cells in 2 mg/ml C (b) and 4 mg/ml C (c). d, e) Comparison of the same disease stage for different collagen concentrations. MSD and α of VGP cells were similar in 2 and 4 mg/ml C (d), whereas MSD and α of MET cells were higher in 2 than 4 mg/ml C (e). Higher MSD and α indicate increased mitochondrial fluctuations and decreased cell stiffness. Error bars omitted for clarity.

2.3.2. VGP and MET cell clusters exhibited similar deformability

The MSD of cell clusters was larger at the MET than the VGP disease stage in 2 mg/ml collagen for short, intermediate, and large delay times. However, the α of VGP and MET clusters were similar. In 4 mg/ml collagen, the MSD and α of VGP and MET clusters were similar.

For VGP clusters, the MSD increased for all τ, whereas α decreased, with increased collagen concentration. A significant reduction in α was detected for $\tau \geq 3$s. A reduction in α indicated that increased collagen concentration stiffened or induced a solid-like response in VGP cells. For the MET stage, the MSD and α of clusters in 2 and 4 mg/ml collagen were similar (Figure 6a).

The advanced disease stage of cell clusters was reflected in increased mitochondrial fluctuations in 2 mg/ml collagen but did not change in 4 mg/ml collagen. The cell stiffness of MET and VGP clusters was similar both in 2 mg/ml and 4 mg/ml collagen (Figure 6b - e). Increased collagen concentration increased mitochondrial fluctuations and cell stiffness in VGP clusters but not in MET clusters.

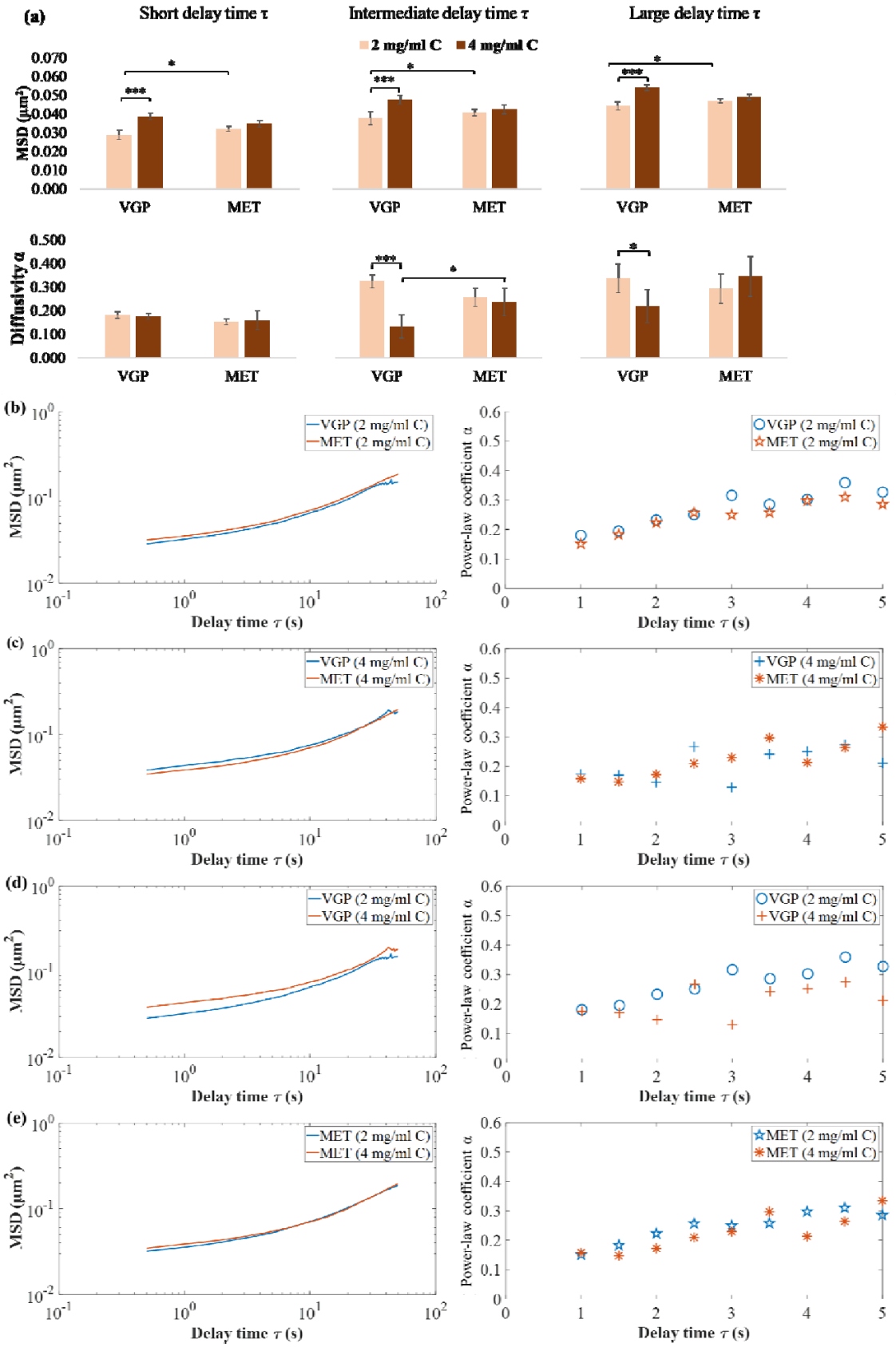
(a)
Short delay time τ
Intermediate delay time τ
Large delay time τ
2 mg/ml C
4 mg/ml C
MSD (μm²)
Diffusivity α
VGP
MET
(b)
VGP (2 mg/ml C)
MET (2 mg/ml C)
(c)
VGP (4 mg/ml C)
MET (4 mg/ml C)
(d)
VGP (2 mg/ml C)
VGP (4 mg/ml C)
(e)
MET (2 mg/ml C)
MET (4 mg/ml C)
MSD (μm²)
Power-law coefficient α
Delay time τ (s)

Figure 6: MSD and power-law coefficient α of VGP and MET ***cell clusters*** *(Day 7) in matrices with 2 and 4 mg/ml collagen concentration (C). a) disease stage and collagen concentration at short (MSD: $\tau = 0.05$ s, α: $\tau = 1$ s), intermediate (MSD and α: $\tau = 3$ s) and long delay time (MSD and α: $\tau = 5$ s). b, c) Comparison of different disease stages for the same collagen concentration. The MSD and power-law coefficient α of VGP clusters were similar to that of MET clusters in 2 mg/ml C (b) and 4 mg/ml C (c). d, e) Comparison of the same disease stage for different collagen concentrations. For VGP clusters, the MSD was smaller, and α was larger in 2 mg/ml C than in 4 mg/ml C (d). MET clusters did not exhibit differences in MSD and α in 2 and 4 mg/ml C (e).*

2.3.3. Mitochondrial fluctuations increased with cluster formation, except for VGP cells in soft matrices

Active processes such as molecular motor activity, prevalent during larger delay times (Mak et al., 2014), typically drive mitochondrial fluctuations into diffusive regimes (Guo et al., 2014). Our results did not indicate significant effects of such active processes for the selected delay times since the mitochondrial fluctuations of cells before and after cluster formation were strongly sub-diffusive ($\alpha \leq 0.3$).

Comparison of MSD data during the onset of cluster formation in 2 mg/ml collagen revealed that the MSD and α of VGP clusters (Day 7) were similar to that of isolated VGP cells (Day 1) for all τ (Figure 7a). For MET cells, the MSD increased, but α did not change while isolated cells evolved into cell clusters (Figure 7b).

In 4 mg/ml collagen, the MSD was larger for VGP clusters than for isolated VGP cells for $\tau <$ 10 s. However, the MSD converged for the largest delay times considered. The power-law coefficient α of VGP clusters were smaller than that of isolated VGP cells for $\tau > 1$ s (Figure 7c). The MSD of MET cells increased with cluster formation, but unlike VGP cells, diverged for the largest delay times. The power-law coefficient α of MET clusters was larger than that of isolated MET cells for all τ (Figure 7d). Decreased α in VGP and increased α in MET cells indicated that VGP cells stiffened, whereas MET cells softened during cluster formation.

In summary, the onset of cluster formation in 2 mg/ml collagen led to increased mitochondrial fluctuations of MET cells but did not affect VGP cells. Further, similar α indicated that cells were equally stiff before and after cluster formation. In contrast, cluster formation in 4 mg/ml collagen generally led to increased mitochondrial fluctuations of VGP and MET cells. However, the cell stiffness of VGP cells increased, whereas that of MET cells decreased (Figure 7).

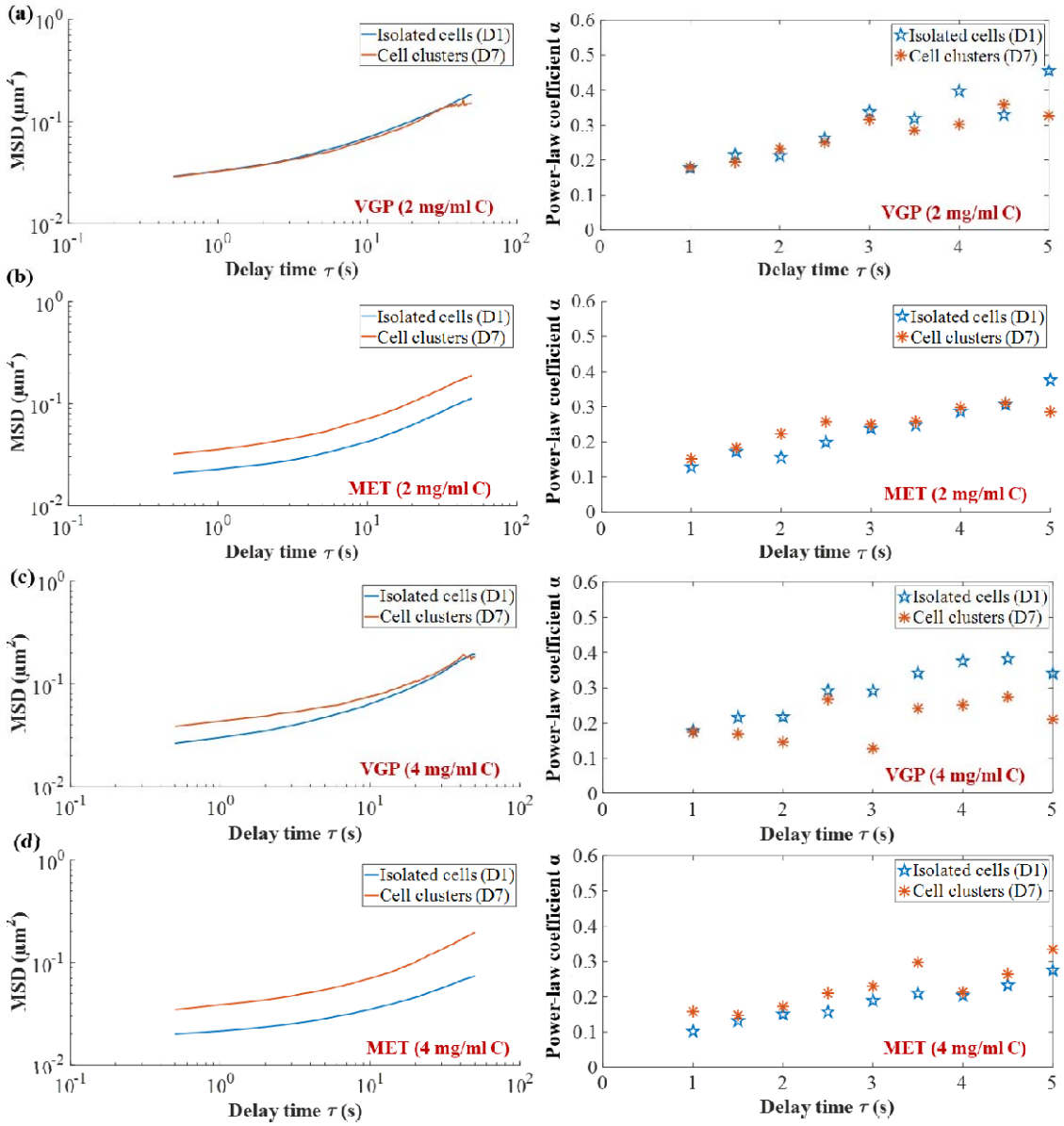

Figure 7: MSD and power-law coefficient α of ***isolated cells*** *and* ***cell clusters*** *in 2 mg/ml (a, b) and 4 mg/ml collagen (C) matrices (c, d) to illustrate the effect of cluster formation on intracellular microrheological properties. In 2 mg/ml collagen, the MSD and α of VGP isolated cells were similar to those of VGP cell clusters (a). For MET cells, the MSD was larger for clusters than for isolated cells, whereas α did not change (b). In 4 mg/ml collagen, VGP clusters exhibited larger MSD and α than isolated VGP cells (c). For MET cells, MSD substantially increased, but α decreased during cluster formation (d). (D1 = Day 1 and D7 = Day 7. Error bars omitted for clarity.)*

2.4. Expression of oncogenic factor TBX3

TBX3 belongs to the T-box family of transcription factors with fundamental roles in development, cell fate and tissue homeostasis (Kumar et al., 2014). However, overexpression

of TBX3 has been implicated in several cancers where it is crucial for cell migration and tumour formation (Khan et al., 2020).

For immunofluorescence assessment, TBX3 of at least nine isolated cells (at Day 1) and nine cell clusters (at Day 7), for n = 2 experiments, were stained, and cell nuclei were counterstained (Figure 8). Nuclear TBX3 was measured.

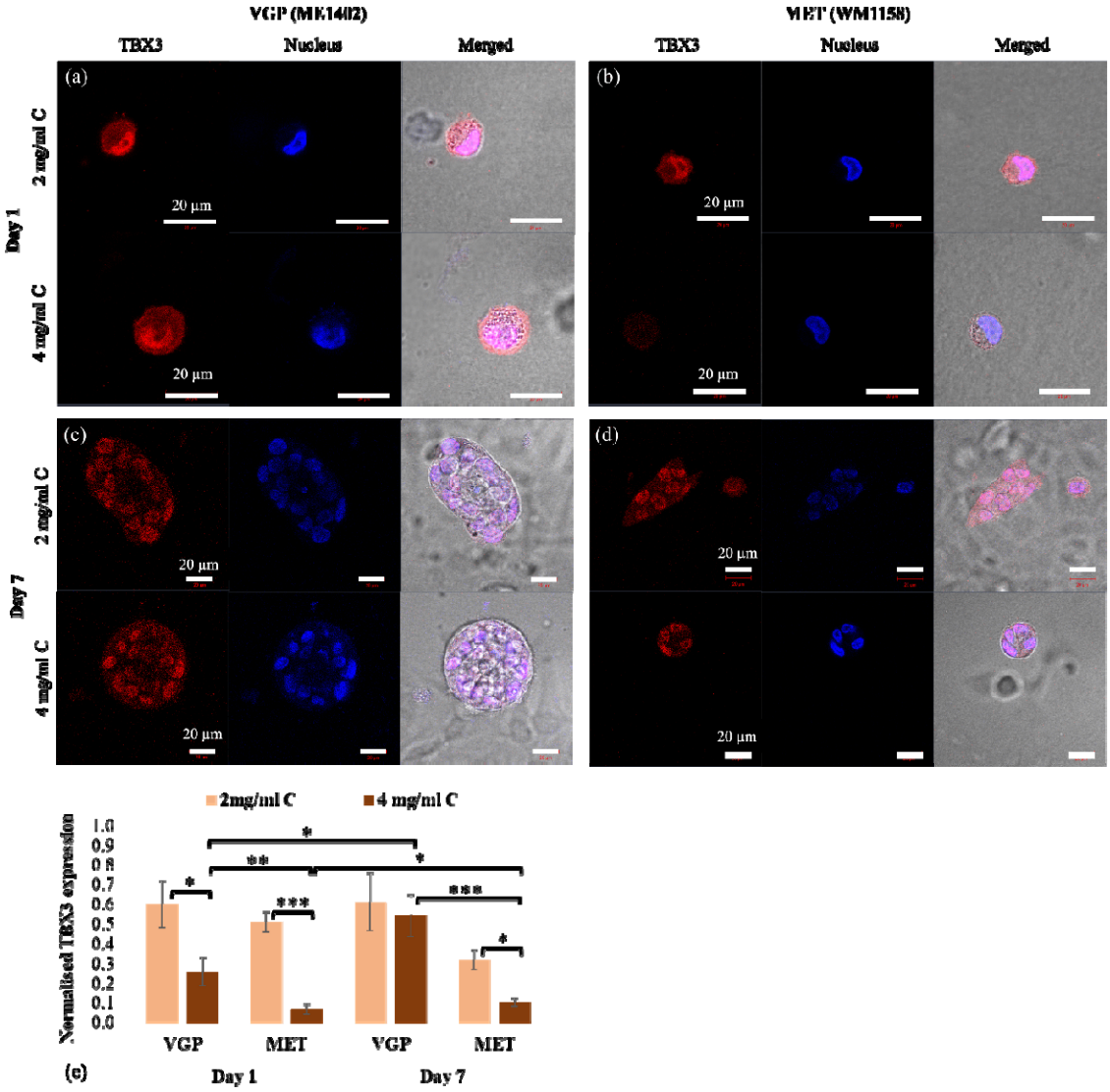

Figure 8: Fluorescent confocal images of TBX3 (red, left column), nucleus (blue, middle column) and merged TBX3 and nucleus superimposed on brightfield images (right column) for VGP and MET cells in 2 and 4 mg/ml collagen matrices after 24 hrs and 7 days (a – d). In merged TBX3 and nucleus fluorescence, pink colour indicates colocalization of TBX3 in the nucleus. (a, b): For isolated cells, TBX3 was expressed in the nuclei of VGP cells in 2 and 4 mg/ml collagen (a) and the nuclei of MET cells in 2 mg/ml collagen but not in 4 mg/ml collagen (b). (c, d): For cell clusters, TBX3 was expressed in the nuclei of VGP clusters in 2 and 4 mg/ml collagen (c) and nuclei of MET clusters in 2 and 4 mg/ml collagen (d). For each condition, sample size was N = 9 from n = 2 repeat experiments. Mid-2D focal plane, 63x magnification, scale bar represents 20 µm.
*(e): Fluorescence of TBX3 normalized to nuclei. For isolated cells (Day 1), TBX3 was overexpressed in VGP and MET cells in 2 mg/ml collagen but decreased with increased collagen concentration. In 4 mg/ml collagen, TBX3 was expressed in isolated VGP cells but absent in MET cells. For cell clusters (Day 7), TBX3 in VGP was equally overexpressed in 2 and 4 mg/ml collagen. In MET clusters, TBX3 was expressed but lower in 4 mg/ml than 2 mg/ml collagen. (Statistical analyses were performed on the logarithmic transformation of normalized TBX3 data since untransformed data were not normally distributed; *** $p < .001$, ** $p < .005$ and * $p < .05$.)*

2.4.1. TBX3 in isolated cells was overexpressed in soft but not in stiff matrices

TBX3 was equally overexpressed in isolated VGP and MET cells in 2 mg/ml collagen ($p = .987$) (Figure 8e, Day 1). Compared to 2 mg/ml collagen, in 4 mg/ml collagen cellular TBX3 levels decreased by 57% ($p = .007$) for VGP and by 87% ($p < .001$) for MET cells. Notably, TBX3 was still detectable and present in VGP cells but nearly disappeared in MET cells in 4 mg/ml collagen.

2.4.2. TBX3 decreased with increased collagen concentration in MET but not VGP cell clusters

In cell clusters, TBX3 levels for MET were 48% lower than for VGP in 2 mg/ml collagen ($p = .344$, non-significant) and 81% lower than for VGP in 4 mg/ml collagen ($p < .001$) (Figure 8e, Day 7). TBX3 of MET clusters was 68% lower in 4 mg/ml than in 2 mg/ml collagen ($p = .006$) whereas TBX3 in VGP clusters was equally overexpressed in 2 and 4 mg/ml collagen ($p = .877$).

2.4.3. TBX3 increased during cluster formation in stiff but not soft matrices

TBX3 levels during VGP cluster formation (i.e. transition from isolated cells at Day 1 to cell clusters at Day 7) increased for 4 mg/ml collagen ($p = .028$) but did not change for 2 mg/ml collagen ($p = .731$) (Figure 8e). For MET cluster formation, TBX3 levels increased in 4 mg/ml collagen ($p = .032$) and decreased in 2 mg/ml collagen ($p = .201$, non-significant).

3. Discussion

We quantified and compared *in vitro* the morphology, intracellular mechanics and TBX3 expression in VGP and MET melanoma cells in isolation and cell aggregates following cluster formation over 10 days in 3D collagen matrices of two different rigidities.

3.1. Isolated cells

Compared to VGP cells, MET cells exhibited smaller volume and mitochondrial fluctuations but higher stiffness in soft and stiff 3D collagen matrices. This reflects evolutionary changes associated with melanoma disease progression. Regulation of cell volume has important biomechanical and biochemical implications. For example, reports have shown that reduced cell volume increases cell stiffness (Guo et al., 2017) and molecular crowding (Miermont et al., 2013), hindering protein mobility and ultimately slowing several biochemical cascades. Importantly, we observed increased stiffness of melanoma cells in the more advanced MET disease stage than in the VGP stage. This contrasts several studies that report decreased stiffness with melanoma disease progression (Omidvar et al., 2014; Pachenari et al., 2014; Xu et al., 2012). However, these studies did not consider the effect of the change in cell volume. Few studies have reported increased stiffness with increased metastatic potential in prostate (Bastatas et al., 2012; Faria et al., 2008) and melanoma cancers (Weder et al., 2014).

It is important to note that VGP cells formed clusters, whereas MET cells predominantly invaded the 3D collagen matrices in isolation. It is recognized that the size and deformability of cancer cells may facilitate penetration through several barriers for secondary colonization (Pachenari et al., 2014). However, VGP cells are yet to penetrate thick layers of skin and need mechanical reinforcement to do so (Bobrowska et al., 2019). It is proposed that the deformability of the large VGP cells is insufficient to allow isolated cells to invade the dermis efficiently. Instead, large cluster formation may serve as a more efficient alternative to invade the surrounding tissue than single-cell invasion.

Furthermore, the Warburg effect can explain the decreased mitochondrial fluctuations in MET compared to VGP cells. In tumour cells, mitochondrial ATP production is insufficient, enabling the switch from mitochondrial to glycolytic metabolic pathways to meet the cell's energy demands (Gogvadze et al., 2008). Interestingly, a strong correlation between glycolytic ATP production and metastatic potential has been reported (Weinberg and Chandel, 2015). Glycolysis is primarily mediated and enhanced by the PI3K/AKT biochemical cascade (Fogg et al., 2011), and PI3K/AKT signalling has been implicated in

melanoma formation and invasion (Peres et al., 2010; Peres and Prince, 2013). It is proposed that reduced mitochondrial fluctuations on account of increased cytoplasmic stiffness may amplify AKT expression by activating glycolytic-mediated metabolism, thereby leading to the rapid and aggravated progression of melanoma. TBX3 was shown to be a substrate of AKT3, an isoform of AKT, and therefore plays prominent roles in the PI3K/AKT signalling pathway to mediate, in part, migration downstream of the PI3K/AKT (Peres et al., 2015).

Our results showed TBX3 overexpression in isolated VGP and MET cells in soft matrices. As previously mentioned, VGP cells quickly formed cell clusters, whereas MET cells mostly remained as isolated cells over time. Considering that TBX3 promotes tumour formation and metastasis (Khan et al., 2020), it is suggested that overexpressed TBX3 promotes migration and cluster formation in isolated VGP cells and migration but not cluster formation in MET cells.

Compared to the overexpressed intracellular TBX3 levels in soft matrices, TBX3 content was 2.3-fold lower in VGP cells and absent in MET cells in the stiff collagen matrix. These results indicate that TBX3 is, in part, governed by the cell's mechanical interaction with its environment and the crucial signalling molecules (Khan *et al.* 2020). Specifically, it is proposed that increased matrix rigidity increases actomyosin contractility, which in turn stimulates signalling molecules that have overlapping functions in cytoskeletal remodelling and the PI3K/AKT signalling pathway. Actomyosin contractility is primarily mediated by Rho GTPases, such as RhoA, Rac1 and Cdc42 (Sipes et al., 2011). Interestingly, it has been reported that Cdc42 activity decreases with increased collagen matrix rigidity (Kim et al., 2014) and that upregulation of the PI3K/AKT pathway correlates with decreased Cdc42 levels (Arias-Romero and Chernoff, 2013).

Cell stiffness increased for isolated MET cells but did not change for VGP cells with increased matrix rigidity. Recent studies have shown that increased matrix rigidity through increased collagen concentration contributes to decreased cell stiffness of isolated prostate (Baker et al., 2009) and breast cancer cells (Kim et al., 2018) in 3D environments. However, using cell lines from various stages of breast, colon, and pancreas cancers, Wullkopf et al. (2018) showed that the cell stiffness of early-stage cancer cells was consistently unaffected by changes in matrix rigidity. In contrast, the cell stiffness of highly metastatic cells either increased or decreased, even within the same cancer type. For example, the cell stiffness of metastatic breast cancer MDA-MB-231 cells increased, whereas the stiffness of 4T1

metastatic breast cancer cells decreased with increased matrix rigidity (Wullkopf et al., 2018).

The VGP cells' inability and the MET cells' ability to adjust their intracellular biomechanics in response to external cues agree in part with the results of Wullkopf et al. (2018). However, it is essential to note that the dissimilarity of VGP and MET cells in adjusting their mechanical properties may be rooted in the functional interaction between cell volume and the extracellular environment. In soft matrices, VGP cells were approximately double the size of MET cells. Accordingly, increased matrix rigidity condensed the volume of large VGP and small MET cells by 11.4 and 5.9%, respectively. Due to the large size, the VGP cells' compression may not immediately affect intracellular traffic, mitochondrial fluctuations, and cell stiffness. In contrast, intracellular traffic was innately confined in small MET cells in soft matrices. Condensation of MET cell size through increased matrix rigidity further compromised intracellular traffic.

3.2. Cluster formation and cell clusters

The onset of cluster formation for VGP cells was associated with changes in intracellular mechanical properties in rigid matrices but not in compliant matrices. In the soft collagen matrices, the mitochondrial fluctuations and cell stiffness of VGP cell clusters (Day 7) were the same as that of isolated cells (Day 1). This steadiness of the intracellular properties suggests that VGP cells were innately endowed with suitable mechanical properties to form clusters in soft matrices. Cluster formation appeared as an automatic cell fate of VGP cells.

The similarity of TBX3 levels in isolated VGP cells and VGP cell clusters supports the innate endowment of VGP cells with essential internal machinery for cluster formation. Based on the established role of TBX3 in promoting tumour formation and metastasis (Khan et al., 2020), we propose that TBX3 overexpression in VGP cell clusters was imperative to mediate their collective migratory modes and the merging with adjacent clusters (see Figure 3). Further, VGP clusters in soft and stiff matrices were similar in cluster size (although different in shape) and, more importantly, in TBX3 expression. Remarkably, Li et al. (2018) demonstrated a strong correlation between TBX3 expression and tumour size.

Our findings of the increase of mitochondrial fluctuations and cell stiffness during VGP cluster formation, i.e. compared to isolated cells, are substantiated by previous studies. Mih et al. (2012) showed that increased matrix rigidity fosters increased proliferative conditions for the cell, and Cheng et al. (2014) associated increased proliferation with increased

mitochondrial activity. The increase in mitochondrial fluctuations may, as such, be a direct consequence of the increased mitochondrial metabolism required for proliferation as VGP cells form clusters in stiff matrices. Cluster growth through proliferation amplifies the compressive environmental conditions, thereby stiffening the VGP cells.

In stiff matrices, VGP and MET cell clusters exhibited increased TBX3 expression compared to low and absent TBX3 expression, respectively, in isolated VGP and MET cells. Thus, increased expression demonstrates that TBX3 is indispensable during cluster formation in stiff environments.

It is also suggested that TBX3 enhances cluster formation through cell proliferation in stiff environments, considering that these environments facilitate an increased proliferative activity of cells (Mih et al., 2012). Previous studies have argued that TBX3 promotes cell migration but impedes proliferation in pancreatic ductal adenocarcinomas, melanoma and breast cancers in 2D *in vitro* and in *in vivo* animal environments (Perkhofer et al., 2016). However, 2D *in vitro* conditions have limited physiological relevance (Kim et al., 2018). Cells exhibit excessive proliferation and cell spreading in 2D compared to 3D environments, stemming from upregulated biochemical signalling that coordinate cell cycling and cell metabolism (Reynolds et al., 2017). *In vivo* animal models better represent human physiological conditions (Kim et al., 2018) but pose challenges for the controlled variation of matrix rigidity and differentiation of metastatic dissemination mode (Cavo et al., 2016).

MET cell cluster formation was associated with increased mitochondrial fluctuations in soft and stiff matrices and decreased cell stiffness in stiff but not in soft matrices. Conceivably, the formation of MET clusters is an energy-demanding process regardless of matrix rigidity. Noting that mitochondrial activity in isolated MET cells was deemed bioenergetically insufficient for cluster formations, the latter was not an automatic cell fate. Instead, cells preferred a more accessible and energy-efficient mechanism, i.e. remaining in isolation, to invade the 3D matrices.

Advanced melanoma metastasizes to several organs in the body, including lung, liver, brain and bone, with different environmental stiffnesses. Our finding that the intracellular stiffness changed during cluster formation in stiff but not in soft matrices suggests that soft matrices provide a more favourable environment for cluster growth. Interestingly, this aligns with clinical and biopsy reports indicating that lungs with soft tissue are often the first and the most common distant melanoma metastasis target (Damsky et al., 2010). Differences in

TBX3 expression in melanoma cells in 3D environments of different stiffness observed in this study may have important implications for developing therapeutic approaches. Melanoma therapies that inhibit TBX3 overexpression may be effective in soft lung tissue but prove ineffective in stiff bone tissue. The change of intracellular stiffness and TBX3 expression in melanoma cells during cluster formation in differently stiff environments demonstrate the need to consider mechanical and molecular biomarkers of cancer malignancy in combination in a tissue-specific context.

4. Materials and methods

4.1. Cell seeding

Advanced human melanoma cell lines, ME1402 vertical growth phase (VGP) and WM1158 metastatic (MET), were cultured using RPMI 1640 media (Life Technologies), supplemented with 10% foetal bovine serum (FBS) and 1% penicillin-streptomycin. Before passaging or experimentation, cells were grown to near confluence in 25 cm^2 tissue flasks (Costar, Corning Life Science, Acton, MA) at 37°C and 5% CO_2. Media was replaced every 3-4 days.

4.2. Collagen embedding

Single cells were embedded in 2 and 4 mg/ml collagen solutions. Collagen solutions comprised Type I Rat Tail Collagen (BD Biosciences, stock solution of 8.21 mg/ml) and neutralizing solution (100 mM HEPES in 2X PBS with pH 7.3) in a 1:1 ratio, diluted with 1XPBS to final concentrations of 2 and 4 mg/ml collagen. For each condition, 50 µl of unpolymerized collagen solution was placed on glass-bottom dishes and incubated at 37°C and 5% CO_2 for 1 hr. After gels polymerized, 500 µl media were added to the wells.

4.3. Morphological assessment

Cellular morphology was assessed on Day 1 for isolated cells and Days 4, 7 and 10 for cell clusters. Media was replaced every three days. Phase-contrast images of cells were acquired on a Zeiss LSM 880 with Airyscan confocal microscope (Carl Zeiss Microimaging, Germany) with a 63x 1.4 oil immersion objective and an electron-multiplying CCD camera (Hamamatsu Photonics, Hamamatsu, Japan). Cells or cell clusters located near the middle of the gel were imaged. At least 28 images were acquired per condition from three repeat experiments (n = 4).

Images were post-processed and morphometrically assessed using Image J (Schindelin et al., 2012) to quantify cell area A and roundness $R = 4A/(\pi \cdot L_M^2)$, where L_M refers to the length of the cell along the major axis. Higher values of R represented rounder shapes. Isolated cells and cell clusters were considered round for $R \geq 0.80$ and elongated for $R < 0.80$.

4.4. Mitochondrial particle tracking microrheology

Microrheology experiments were conducted on isolated cells on Day 1 and cell clusters on Day 7. Mitochondria were fluorescently labelled 1 hr before experimentation by incubating cells with 350 nM Mitotracker Green solution (Life Technologies, Carlsbad, CA) added to RPMI 1640 media. Cells and cell clusters near the middle of the collagen gel were imaged in time-lapse mode (50 ms per frame for 120 s) to capture mitochondrial fluctuations. Time-lapse images were collected with a Zeiss LSM 880 with Airyscan confocal microscope (Carl Zeiss Microimaging, Germany) with 63x 1.4 oil immersion objective and an electron-multiplying CCD camera (Hamamatsu Photonics, Hamamatsu, Japan). Experiments were repeated at least once (n = 2), each time assessing at least 24 isolated cells per condition and 16 cell clusters. At least four outer cells per cluster were assessed.

For analysis, time-lapse images of cells with at least 60 mitochondria and each mitochondrion visible for at least 80% of the total acquisition time were used. Mitochondrial particle trajectories were constructed in TrackMate (Tinevez et al., 2017) and converted to the mean square displacement (MSD) using @msdanalyzer (Tarantino et al., 2014) in MATLAB (The MathWorks, Natick, MA).

The ensemble-averaged MSD $\langle \Delta r^2 (\tau)_{xy} \rangle$ was calculated according to:

$$\langle \Delta r^2(\tau)_{xy} \rangle = \langle [x(t+\tau) - x(t)] + [y(t+\tau) - y(t)] \rangle^2. \quad (1)$$

Here, τ is the delay time between the first and last image frame used for the analysis, and x(t) and y(t) are the spatial coordinates of mitochondrial particle positions at time t.

For viscoelastic materials, the MSD scales nonlinearly with τ according to a power-law relationship, $\langle \Delta r^2 (\tau)_{xy} \rangle \sim \tau^{\alpha}$. The MSD-dependant power-law coefficient α was determined as a measure of intracellular fluidity (deformability):

$$\alpha = \frac{\partial \ln \langle \Delta r^2(\tau) \rangle}{\partial \ln(\tau)} . \quad (2)$$

4.5. Immunofluorescent quantification of TBX3 and F-actin

Cells were stained for either TBX3 on Day 1 and 7 or F-actin on Day 7 as previously described (Artym and Matsumoto, 2010). In brief, cells were gently washed with PBS and fixed with 4% paraformaldehyde in PBS at room temperature for 20 min. Cells were washed thrice with PBS and permeabilized with 0.2% Triton X-100 in PBS at room temperature for 10 min. Cells were blocked in 5% sheep serum in PBS for 1 hr at room temperature and washed once with PBS/Tween. For TBX3 staining, cells on Day 1 and cell clusters on Day 7 were incubated overnight at 4°C with rabbit polyclonal anti-TBX3 antibody (Zymed 42-4800, Zymed Laboratories) at a 1:50 dilution in 5% sheep serum. Next, cells were washed thrice with PBS/Tween, incubated with Cy3 donkey anti-rabbit IgG (Jackson ImmunoResearch Laboratories, Inc., USA) at a dilution of 1:1000 for 60 min and washed thrice more with PBS/Tween. For actin staining, cell clusters on Day 7 were incubated overnight with 100 nM Acti-stain™ 488 Phalloidin (Cat. #PHDG1, Cytoskeleton Inc., USA) and washed thrice with PBS. Nuclei were counterstained with 1 µg/ml Hoechst (Sigma, USA) for 10 min and finally washed thrice in PBS before imaging.

A series of confocal cross-sectional images with a constant step size of 0.5 µm (z-stack) per cell cluster was acquired (Zeiss LSM 880 AiryScan microscope, 63x 1.4 oil immersion objective) and converted to a single image employing the maximum intensity projection (MIP) (ZEN lite black edition, Zeiss, Germany). The fluorescence in MIP images was quantified as the corrected total cell fluorescence CTCF = $I - A_{\mathrm{ROI}} \cdot b$, where I is the integrated pixel density (sum of all pixels) of the region of interest for fluorescence quantification, A_{ROI} is the area of the region of interest, and b is the mean fluorescence of the background in the region of interest (Gavet and Pines, 2010).

The schedule of the experimental activities and assessments is summarised in the supplemental Table S2.

4.6. Statistical analysis

The normality of data was evaluated using the Shapiro-Wilk test. Data were reported as mean ± standard deviation in the text and mean and standard error of the mean (SEM) in graphs. All evaluations used $p < .05$ for statistical significance unless otherwise stated, e.g., for multiple comparisons.

Regression models determined whether disease stage, collagen matrix concentration and time point of the experiments were predictors of area and roundness of isolated cells and cell clusters. For area measurements, multiple linear regression models were derived to predict the cluster size as either absolute area, $\hat{A}$, or as area normalized to the mean single-cell area, $\hat{A}_N$. Beta regression models were employed to predict the roundness □.

Microrheology, TBX3 and F-actin data were assessed with multi-factorial ANOVA for significant main effects and two- or three-way interactions among variables. Significant interactions were further assessed with linearly independent pairwise comparisons among estimated marginal means.

Statistica for Windows (Version 13.5, TIBCO Software Inc., Palo Alto, CA) was used for regression model analysis, and SPSS for Windows (Version 25, IBM Corp., Armonk, NY) was used for all other analyses.

List of symbols

A	Area of a cell or cell cluster measured
$\hat{A}$	Area of cell or cell cluster predicted by a regression model
A_N	Normalized area, i.e., measured area of cell or cell cluster normalized to mean single-cell area
$\hat{A}_N$	Normalized area of cell or cell cluster, i.e., area of cell or cell cluster normalized to mean single-cell area, predicted by a regression model
A_{ROI}	Area of the region of interest in image
B	Background signal intensity in an image
I	Integrated pixel density
L_M	Length of a cell along its major axis
n	Number of biological repeats
N	Sample size
p	Indicator of statistical significance
R	Roundness of a cell or cell cluster measured
□	Roundness of a cell or cell cluster predicted by a regression model
r	Mitochondrial displacement
t	Time
α	Power law coefficient
τ	Delay time, lag time in mean square displacement analysis

Data

Data supporting the results presented in this article are available on the University of Cape Town's institutional data repository (ZivaHub) under http://doi.org/10.25375/uct.14254394.

Acknowledgements

We acknowledge the technical assistance of Mrs Susan Cooper of the Confocal and Light Microscope Imaging Facility of the University of Cape Town. The microscope used in this work was purchased with funds from the Wellcome Trust (grant number 108473/Z/15/Z) and the National Research Foundation of South Africa (grant number UID93197). Ms Anneli Hardy from the Statistical Consulting Service at the Department of Statistical Sciences, University of Cape Town, is acknowledged for conducting the regression model analysis.

Conflicts of interest

The authors declare that they have no conflicts of interest.

Funding sources

This study was supported financially by the National Research Foundation of South Africa (grant number IFR14011761118 to TF and grant number SRUG190306422357 to SP), the South African Medical Research Council (TF and SP), the Cancer Association of South Africa (SP), and the University of Cape Town (TF and SP). The funders had no role in study design, data collection and analysis, decision to publish, or preparation of the manuscript. Any opinion, findings and conclusions or recommendations expressed in this publication are those of the authors and do not necessarily represent the official views of the funding agencies.

References

Agus, D. B., Alexander, J. F., Arap, W., Ashili, S., Aslan, J. E., Austin, R. H., Backman, V., Bethel, K. J., Bonneau, R., Chen, W.-C. et al. (2013). A physical sciences network characterization of non-tumorigenic and metastatic cells. *Sci Rep* **3**, 1449.

Arias-Romero, L. E. and Chernoff, J. (2013). Targeting Cdc42 in cancer. *Expert Opin Ther Targets* **17**, 1263-73.

Artym, V. V. and Matsumoto, K. (2010). Imaging cells in three-dimensional collagen matrix. *Curr Protoc Cell Biol* **Chapter 10**, Unit 10 18 1-20.

Baker, E. L., Bonnecaze, R. T. and Zaman, M. H. (2009). Extracellular matrix stiffness and architecture govern intracellular rheology in cancer. *Biophysical Journal* **97**, 1013-21.

Bastatas, L., Martinez-Marin, D., Matthews, J., Hashem, J., Lee, Y. J., Sennoune, S., Filleur, S., Martinez-Zaguilan, R. and Park, S. (2012). AFM nano-mechanics and calcium dynamics of prostate cancer cells with distinct metastatic potential. *Biochim Biophys Acta* **1820**, 1111-20.

Bobrowska, J., Awsiuk, K., Pabijan, J., Bobrowski, P., Lekki, J., Sowa, K. M., Rysz, J., Budkowski, A. and Lekka, M. (2019). Biophysical and biochemical characteristics as complementary indicators of melanoma progression. *Anal Chem* **91**, 9885-9892.

Cavo, M., Fato, M., Penuela, L., Beltrame, F., Raiteri, R. and Scaglione, S. (2016). Microenvironment complexity and matrix stiffness regulate breast cancer cell activity in a 3D in vitro model. *Sci Rep* **6**, 35367.

Cheng, G., Zielonka, J., McAllister, D., Tsai, S., Dwinell, M. B. and Kalyanaraman, B. (2014). Profiling and targeting of cellular bioenergetics: inhibition of pancreatic cancer cell proliferation. *Br J Cancer* **111**, 85-93.

Chugh, P. and Paluch, E. K. (2018). The actin cortex at a glance. *J Cell Sci* **131**.

Damsky, W. E., Rosenbaum, L. E. and Bosenberg, M. (2010). Decoding melanoma metastasis. *Cancers* **3**, 126-63.

Faria, E. C., Ma, N., Gazi, E., Gardner, P., Brown, M., Clarke, N. W. and Snook, R. D. (2008). Measurement of elastic properties of prostate cancer cells using AFM. *Analyst* **133**, 1498-500.

Fife, C. M., McCarroll, J. A. and Kavallaris, M. (2014). Movers and shakers: cell cytoskeleton in cancer metastasis. *Br J Pharmacol* **171**, 5507-23.

Fogg, V. C., Lanning, N. J. and Mackeigan, J. P. (2011). Mitochondria in cancer: at the crossroads of life and death. *Chin J Cancer* **30**, 526-39.

Gavet, O. and Pines, J. (2010). Progressive activation of CyclinB1-Cdk1 coordinates entry to mitosis. *Dev Cell* **18**, 533-43.

Gogvadze, V., Orrenius, S. and Zhivotovsky, B. (2008). Mitochondria in cancer cells: what is so special about them? *Trends Cell Biol* **18**, 165-73.

Guo, M., Ehrlicher, A. J., Jensen, M. H., Renz, M., Moore, J. R., Goldman, R. D., Lippincott-Schwartz, J., Mackintosh, F. C. and Weitz, D. A. (2014). Probing the stochastic, motor-driven properties of the cytoplasm using force spectrum microscopy. *Cell* **158**, 822-832.

Guo, M., Pegoraro, A. F., Mao, A., Zhou, E. H., Arany, P. R., Han, Y., Burnette, D. T., Jensen, M. H., Kasza, K. E., Moore, J. R. et al. (2017). Cell volume change through water efflux impacts cell stiffness and stem cell fate. *Proc Natl Acad Sci U S A* **114**, E8618-E8627.

Khan, S. F., Damerell, V., Omar, R., Du Toit, M., Khan, M., Maranyane, H. M., Mlaza, M., Bleloch, J., Bellis, C., Sahm, B. D. B. et al. (2020). The roles and regulation of TBX3 in development and disease. *Gene* **726**, 144223.

Kim, J. E., Reynolds, D. S., Zaman, M. H. and Mak, M. (2018). Characterization of the mechanical properties of cancer cells in 3D matrices in response to collagen concentration and cytoskeletal inhibitors. *Integr Biol (Camb)* **10**, 232-241.

Kim, S. J., Wan, Q., Cho, E., Han, B., Yoder, M. C., Voytik-Harbin, S. L. and Na, S. (2014). Matrix rigidity regulates spatiotemporal dynamics of Cdc42 activity and vacuole formation kinetics of endothelial colony forming cells. *Biochem Biophys Res Commun* **443**, 1280-5.

Kumar, P. P., Franklin, S., Emechebe, U., Hu, H., Moore, B., Lehman, C., Yandell, M. and Moon, A. M. (2014). TBX3 regulates splicing in vivo: a novel molecular mechanism for Ulnar-mammary syndrome. *PLoS Genet* **10**, e1004247.

Li, Z., Wang, Y., Duan, S., Shi, Y., Li, S., Zhang, X. and Ren, J. (2018). Expression of TBX3 in hepatocellular carcinoma and Its clinical implication. *Med Sci Monit* **24**, 9324-9333.

Mak, M., Kamm, R. D. and Zaman, M. H. (2014). Impact of dimensionality and network disruption on microrheology of cancer cells in 3D environments. *PLoS Comput Biol* **10**, e1003959.

Mason, T. G., Ganesan, K., van Zanten, J. H., Wirtz, D. and Kuo, S. C. (1997). Particle Tracking Microrheology of Complex Fluids. *Physical Review Letters* **79**, 3282-3285.

Mierke, C. T., Rosel, D., Fabry, B. and Brabek, J. (2008). Contractile forces in tumor cell migration. *European Journal of Cell Biology* **87**, 669-76.

Miermont, A., Waharte, F., Hu, S., McClean, M. N., Bottani, S., Leon, S. and Hersen, P. (2013). Severe osmotic compression triggers a slowdown of intracellular signaling, which can be explained by molecular crowding. *Proc Natl Acad Sci U S A* **110**, 5725-30.

Mih, J. D., Marinkovic, A., Liu, F., Sharif, A. S. and Tschumperlin, D. J. (2012). Matrix stiffness reverses the effect of actomyosin tension on cell proliferation. *J Cell Sci* **125**, 5974-83.

Northcott, J. M., Dean, I. S., Mouw, J. K. and Weaver, V. M. (2018). Feeling stress: the mechanics of cancer progression and aggression. *Front Cell Dev Biol* **6**, 17.

Omidvar, R., Tafazzoli-Shadpour, M., Shokrgozar, M. A. and Rostami, M. (2014). Atomic force microscope-based single cell force spectroscopy of breast cancer cell lines: an approach for evaluating cellular invasion. *J Biomech* **47**, 3373-9.

Pachenari, M., Seyedpour, S. M., Janmaleki, M., Babazadeh Shayan, S., Taranejoo, S. and Hosseinkhani, H. (2014). Mechanical properties of cancer cytoskeleton depend on actin filaments to microtubules content: investigating different grades of colon cancer cell lines. *J Biomech* **47**, 373-9.

Peres, J., Davis, E., Mowla, S., Bennett, D. C., Li, J. A., Wansleben, S. and Prince, S. (2010). The highly homologous T-box transcription factors, TBX2 and TBX3, have distinct roles in the oncogenic process. *Genes Cancer* **1**, 272-82.

Peres, J., Mowla, S. and Prince, S. (2015). The T-box transcription factor, TBX3, is a key substrate of AKT3 in melanomagenesis. *Oncotarget* **6**, 1821-33.

Peres, J. and Prince, S. (2013). The T-box transcription factor, TBX3, is sufficient to promote melanoma formation and invasion. *Mol Cancer* **12**, 117.

Perkhofer, L., Walter, K., Costa, I. G., Carrasco, M. C. R., Eiseler, T., Hafner, S., Genze, F., Zenke, M., Bergmann, W., Illing, A. et al. (2016). Tbx3 fosters pancreatic cancer growth by increased angiogenesis and activin/nodal-dependent induction of stemness. *Stem Cell Research* **17**, 367-378.

Reynolds, D. S., Tevis, K. M., Blessing, W. A., Colson, Y. L., Zaman, M. H. and Grinstaff, M. W. (2017). Breast cancer spheroids reveal a differential cancer stem cell response to chemotherapeutic treatment. *Sci Rep* **7**, 10382.

Schindelin, J., Arganda-Carreras, I., Frise, E., Kaynig, V., Longair, M., Pietzsch, T., Preibisch, S., Rueden, C., Saalfeld, S., Schmid, B. et al. (2012). Fiji: an open-source platform for biological-image analysis. *Nat Methods* **9**, 676-82.

Sipes, N. S., Feng, Y., Guo, F., Lee, H. O., Chou, F. S., Cheng, J., Mulloy, J. and Zheng, Y. (2011). Cdc42 regulates extracellular matrix remodeling in three dimensions. *J Biol Chem* **286**, 36469-77.

Tarantino, N., Tinevez, J. Y., Crowell, E. F., Boisson, B., Henriques, R., Mhlanga, M., Agou, F., Israel, A. and Laplantine, E. (2014). TNF and IL-1 exhibit distinct ubiquitin requirements for inducing NEMO-IKK supramolecular structures. *J Cell Biol* **204**, 231-45.

Taubenberger, A. V., Girardo, S., Traber, N., Fischer-Friedrich, E., Krater, M., Wagner, K., Kurth, T., Richter, I., Haller, B., Binner, M. et al. (2019). 3D microenvironment stiffness regulates tumor spheroid growth and mechanics via p21 and ROCK. *Adv Biosyst* **3**, e1900128.

Tinevez, J. Y., Perry, N., Schindelin, J., Hoopes, G. M., Reynolds, G. D., Laplantine, E., Bednarek, S. Y., Shorte, S. L. and Eliceiri, K. W. (2017). TrackMate: An open and extensible platform for single-particle tracking. *Methods* **115**, 80-90.

Weder, G., Hendriks-Balk, M. C., Smajda, R., Rimoldi, D., Liley, M., Heinzelmann, H., Meister, A. and Mariotti, A. (2014). Increased plasticity of the stiffness of melanoma cells correlates with their acquisition of metastatic properties. *Nanomedicine* **10**, 141-8.

Weinberg, S. E. and Chandel, N. S. (2015). Targeting mitochondria metabolism for cancer therapy. *Nat Chem Biol* **11**, 9-15.

Wullkopf, L., West, A. V., Leijnse, N., Cox, T. R., Madsen, C. D., Oddershede, L. B. and Erler, J. T. (2018). Cancer cells' ability to mechanically adjust to extracellular matrix stiffness correlates with their invasive potential. *Mol Biol Cell* **29**, 2378-2385.

Xu, W., Mezencev, R., Kim, B., Wang, L., McDonald, J. and Sulchek, T. (2012). Cell stiffness is a biomarker of the metastatic potential of ovarian cancer cells. *PLoS One* **7**, e46609.